Earthquake-induced landslides monitoring and survey by means of InSAR

Tayeb SMAIL[1], Mohamed ABED[1], Ahmed MEBARKI[2,3], Milan Lazecky[4,5]

[1]Department of Civil Engineering, Saad Dahlab University, Blida City, Algeria

[2]Univ Gustave Eiffel, Univ Paris Est Creteil, CNRS, UMR 8208, MSME, 5 Bd Descartes, F-77454 Marne-la-Vallée, France~~University Gustave Eiffel, Laboratory Multi Scale Modeling and Simulation (UMR 8208 CNRS/UPEC/U.Eiffel), 5 Bd Descartes, 77454, Marne-La-Vallee, France~~

[3]Nanjing Tech University, 5 New Mofan Rd, Gulou, Nanjing, Jiangsu, Chine - Permanent Guest Professor within "High-Level Foreign Talents Programme" grant

[4]IT4Innovations, VSB-TU Ostrava, 17, Listopadu 15, 70833 Ostrava-Poruba, Czech Republic

[5]School of Earth and Environment, University of Leeds, Leeds LS2 9JT, UK

Correspondence to: SMAIL Tayeb (st_gc@hotmail.fr)

Abstract. This study uses interferometric SAR techniques to identify and track earthquake-induced landslides ~~landslides and~~ as well as lands prone to landslides, by detecting deformations ~~fringes and changes~~ in areas struck by earthquakes. The pilot study area investigates the Mila region ~~(~~in Algeria,~~)~~ which suffered significant landslides and structural damages (earthquake: Mw~~-~~5, 2020-08-07~~):~~). ~~the study checks ground deformations and tracks earthquake-induced landslides.~~ DInSAR analysis ~~shows~~ shows normal interferograms~~,~~ with ~~atmospheric contribution, and slight~~small fringes.~~ However, i~~ The Coherence Change Detection (CCD) and DInSAR analysis were able to identify many landslides and ground deformations confirmed also by~~In addition, SAR images and~~ Sentinel-2 optical images ~~(Sentinel-2) confirm~~ and ~~site~~ field inspection. The most important displacement (2.5 m), located in Kherba neighborhood, caused ~~causing~~ severe damages to dwellings. It is worth notice that CCD and DInSAR are very useful since they were also able to identify ground cracks surrounding a large zone (3.94 Km^2 area) in Grarem City whereas the Sentinel-2 optical images could not detect them. ~~These unnoticed ground disorders were confirmed during fields inspection. Such results have key importance since they can serve as an alert to monitor the zone at the proper time.~~ Although, ~~Displacement~~ displacement ~~time~~ time-series analysis of 224 ~~many~~ interferograms ~~-~~(~~April~~ 04-2015 to ~~September~~ 09-2020) ~~using LiCSBAS were~~performed using LiCSBAS did not detect any pre-event geotechnical precursors, the post-event analysis shows a 110 mm/y subsidence velocity in the ~~back~~ back-hillside of Kherba~~, and high displacement velocity at specific points in Grarem region~~.

1 Introduction

Although it is still challenging to predict exactly where and when natural hazards (earthquakes, landslides, floods, etc.) might occur, the capacity to monitor and survey the zones prone to important landslides as well as the capacity to identify and locate those impacted by earthquakes are key issues in risks mitigation, reduction, preparedness and adaptation. Actually, since earthquakes and landslides might occur in many places worldwide, they might cause a huge number of victims, important socio-economic, assets damages and losses. Their impact can be significantly reduced thanks to satellite imaging which allows prediction and early alerts of some landslide cases (Jacquemart and Tiampo, 2021; Mazzanti et al., 2012; Moretto et al., 2021).

It is then worth detecting or predicting critical ground changes at specific places, either after a geotechnical ~~disorder~~ hazard occurs due to landslides and earthquakes mainly, or before it is suddenly triggered (Bakon et al., 2014; Galve et al., 2015).

Such challenges can be tackled by regular image processing oriented landslides areas monitoring, in the aftermath of earthquakes, ~~by means of~~using SAR interferometric methods and optical images, for instance. Actually, since ~~In~~SAR (~~Interferometric~~ Synthetic Aperture Radar) is an active sensor system that uses microwave signals to collect data backscattered from the earth's surface, the use of satellite imaging systems like Interferometric ~~In~~SAR methods appears as a cost-effective way for measuring millimeter-level displacements of the earth surface (Herrera et al., 2009), at a regional scale and can be used as an early warning system for the safety of structures and their surroundings (Galve et al., 2015; Roque et al., 2015).

The expected outcomes are based upon the processing of SAR data ~~making use~~as it uses ~~of~~ Differential InSAR (DInSAR), Coherence Change Detection (CCD), and time series analysis (~~using~~ LiCSBAS software). LiCSBAS ~~of that exploit~~exploits the LiCSAR data ~~which is a system for and~~that process ~~processing~~ InSAR datasets automatically ~~automatically~~ (Sentinel-1 ~~dataset~~) ~~using LiCSBAS software~~, ~~to illustrate the~~taking advantage~~s~~ of high-resolution SAR sensing, in order to track ~~for the objective of tracking~~ ground changes and landslides.

The ~~performed~~ SAR analyses ~~can reveal some~~aim to detect ground deformations ~~changes detected~~ through DInSAR and CCD ~~maps~~investigations~~,~~ as they consider, for illustrative purposes, a city in Algeria struck by an earthquake~~as it is shown the illustrative purposes for the 7th of August 2020 earthquake~~ (August 7, 2020: Algeria, Mila): ~~. The~~the ground ~~se~~ deformations and displacements~~displacements~~, ~~which occurred~~ in Kherba City ~~the~~ and ~~northeastern part at the~~ Garem City (northeastern part of Mila downtown, ~~(~~2 km ~~from Mila downtown~~) ~~and Kherba City~~ are investigated~~presented as , caused a loss of coherence in CCD maps and as fringes in DInSAR maps~~. The~~ir extend affects~~ affected areas ~~of around~~span over 3.94 km² for Garem and 2.1 km² for the Kherba landslide~~s area~~case. Furthermore, ~~the~~ a time-series analysis of LiCSAR data performed out by ~~using~~ LiCSBAS software, investigates ~~reveals a slo~~the~~w~~ possible existence of precursors in geotechnical conditions~~subsidence deformation signal in the left part of the other of Kherba landslide side area in the Kherba case~~.

~~The formed fringes and coherence loss in the Garem case indicate the boundary of a potential land failure. The results can serve as early warning information provided by the InSAR monitoring system, since the area should be monitored to investigate the existent of plane failure or probable growing slope failuresdisorder.~~

2 Land and ground movements monitoring and surveying in the aftermath of an earthquake

2.1 Satellite images and methods - Case study

The present research study is multifold. It aims to use InSAR image processing for various purposes, in the case of landslides and earthquakes:

- Use the InSAR in the aftermath of an earthquake in order to identify the geotechnical ~~disorders~~~~hazards~~displacements or deformations, their extent, and locations. The Differential radar interferometry and the Coherence Changes Detection are the most adapted methods for ground and soil surfaces changes detection (Jung and Yun, 2020; Meng et al., 2020; Pawluszek-Filipiak and Borkowski, 2020; Tampuu et al., 2020; Tzouvaras et al., 2020). A city, Mila, in Northern Algeria, is considered as the pilot study. It has been struck by an earthquake in August 2020. The ~~geotechnical hazards disorders (~~landslides and surface ~~faults)~~cracks have been affected significantly, during the ~~same~~ earthquake events series, two distinct zones being distant by almost 15 km from each other (Kherba and Garem).
- Use ~~the~~ time~~-~~series analysis to investigate ~~study~~ the ~~mean~~ displacements and ~~mean displacemen~~theirt ~~velocity~~ velocities before and after the occurrence of the main shock. For the city of Mila, the time series is performed out for a period extending from April 2015 up to October 2020, i.e. a long period before ~~the~~ (~~*April 2015 up to March 2020, i.e.*~~ *5 entire years*) ~~and a period *4 months* ahead of~~ the main shock in order to avoid a disturbance or bias that might be related to seasonal effects such as rains and vegetation effects ~~(Lazecký et al., 2020a).~~(Lazeckẏ et al., 2020a), and a short period (*4 months*) ~~ahead~~ahead of ~~of~~ the event date in order to ~~check~~investigate the historical development of the landslide.
- Compare and correlate the InSAR images processing results with the satellite optical images observations.

2.2 Pilot zone, earthquakes and landslides - Observed disorders

The case study area lies in Mila Province which is located in the northeast part of Algeria (Mediterranean zone), near the Dam of Beni Haroun. The Mediterranean zone is seismically active because of the northward convergence (4-10 mm/yr) of the African plate relative to the Eurasian plate along a complex plate boundary (Frizon de Lamotte et al., 2000; Mouloud and Badreddine, 2017; Peláez Montilla et al., 2003; USGS, n.d.)~~.~~. Throughout the last years, several landslide events have taken place in the wider region of Mila (Merghadi et al., 2018). Merghadi et al.(2018) constructed a detailed landslide inventory map of the study area. The seismic activities and landslides pose a persistent threat for built-up areas and facilities, such as roadways, bridges and tunnels, which need continuous monitoring and survey.

After an earthquake (Mw 5, 2020-08-07, epicenter 36.550° N - 6.271° E, Depth=10 km, (USGS)) that struck this region, important landslides were mostly observed in Mila City and its surroundings, see Figs. 1~~ and 2~~-3. Although, the earthquake was moderate, Beni Haroun Dam and the two large bridges built on the RN 27 highway needs to be inspected and their possible displacements monitored.

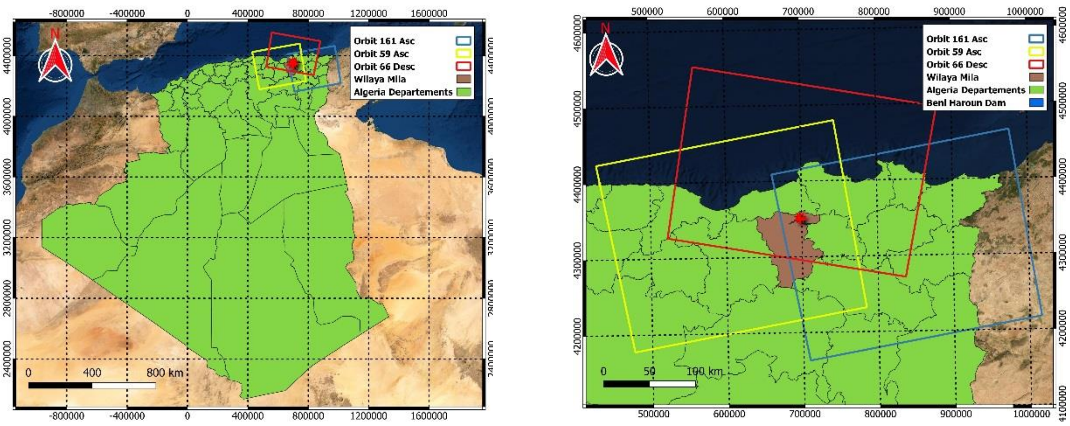

(a) (b)

Figure 1. Mila location map (a), ascending and descending orbits footprints. Red stars indicate earthquake epicenter (QGIS, ESRI basemap).

In the present, two areas are studied, i.e. Kherba and Grarem Cities. The altitude at the top point 1 (Fig. ~~4~~2.a) in Kherba hill is 654 m and~~ in~~ 411 m for the upper point (2)~~ is 411 m a.s.l. in the upper point (2)~~, located at ~~with a horizontal length between ~~2.14 km distance with 11.34% ~~and a ~~slope~~ of 11.34%~~. The maximum ground horizontal offset reached 2.5 m and the vertical deformations exceed 1.8 m (Fig. ~~2~~3.b) at the top of Kherba hill (point A Fig. ~~4~~2.a). The slope failure boundary of Kherba City is mapped as shown in Fig. ~~4~~2.b. The Grarem area of interest (AoI) is located ~~at ~~east north of Mila in ~~a ~~hilly ground with an average slope reaching 12.5%, see Fig. ~~4~~2.c.

(a) (b) (c)

Figure ~~4~~2. 3D view of AoIs, Kherba AoI and Grarem using QGIS with DEM SRTM 1sec and ESRI basemap, a & b are Kherba AoI, c is the Grarem case area, the red polygon is the boundary of change detected by InSAR.

(a) (b) (c)

Figure ~~2~~3. Ground cracks due to landslides in Kherba, Mila, ~2.5m offset towards the North, a. Drone aerial photo from (LNHC), b. & c.- Lateral displacements (*Photos: courtesy M. Yacoub A., University of Setif, Algeria*).

2.3 Pilot zone - Data and images collection

The dataset used for this study is collected from European Space Agency (ESA), via the Copernicus Open Access portal, and from the Alaska Satellite Facility (ASF DAAC). The C-band Sentinel-1 A and B, launched in 2014 and 2016 respectively, provide regular data~~-~~sets~~,~~. ~~t~~The Sentinel-1 sensors have a wavelength of 5.546 cm (ESA), suitable for change detection and monitoring of large areas, and are right side-looking with an incidence angle ranging approximately from 20° to 46° (ESA, 2012)~~, which are suitable for change detection and the monitoring of large areas.~~ ~~(Morishita, 2021).~~ For the InSAR use, the Interferometric Wide (IW) swath Single Look Complex (SLC) data is selected and processed with the open-source software SNAP (Sentinel Applications Platform). It is worth using data from many orbits to monitor the AoIs due to different oriented directions, incidence angles of satellites, and the ground topography. The optical images of Sentinel-2 ~~sensors~~ satellites are obtained from ESA, whereas downloading and processing data is done via QGIS, Semi-Automatic Classification Plugin (SCP) (Congedo, 2021).

For Mila region, the AoI is covered by 3 orbits~~(~~, ~~2~~two are ascending (66, 59) and ~~1~~ one is descending ~~66, 59(, and~~ 161) (Fig. 1). Since the present study intends to detect the areas influenced by landslides, many pre-event and post-event data ~~are~~ were used ~~in order to get an accurate evaluation of the event~~. Eighteen Sentinel-1 A and 17 Sentinel-1 B images (a total of 35) ~~images~~ were downloaded to monitor Mila's area for the period ~~of~~ from 1 July 2020 to 26 October 2020~~, to monitor Mila's area, and are being used to perform out a detailed study on the land deformations and the dynamics of the landslide~~. Table 1 summarizes the appropriate interferograms, i.e. those having ~~with that have a~~ small perpendicular baselines and short temporal baselines. Tables 1, ~~-~~2, and~~-~~ 2bis present~~s~~ all the images, their ~~used in this study and they are labelled as~~labels as IFG-ID, Orbits, and dates of ~~their~~ acquisitions~~summarize the whole data collected for the case study~~.

Table 1. Characteristics of Sentinel-1 InSAR pairs ~~for Mila case~~used for this study.

IFG-ID	Track	M Date	S- Date	*Bp* [m]	*Bt* [days]
IFG-~~1~~0		2020-07-22	2020-07-28	-9.99	6
IFG-1		2020-07-28	2020-08-03	40.90	6
IFG-2		2020-07-28	2020-08-03	40.62	6
IFG-3		2020-08-03	2020-08-09	-51.47	6
IFG-4	**66 ASCENDING**	2020-08-03	2020-08-09	-50.76	6
IFG-5		2020-08-09	2020-08-15	-27.57	6
IFG-6		2020-08-09	2020-08-15	27.62	6
IFG-7		2020-08-15	2020-08-21	-16.19	6
IFG-8		2020-08-21	2020-08-27	42.43	6

IFG-9		2020-08-27	2020-09-02	-28.59	6
IFG-10		2020-09-02	2020-09-08	29.26	6
IFG-11		2020-09-08	2020-09-14	17.95	6
IFG-12		2020-09-14	2020-09-20	-6.05	6
IFG-13		2020-09-20	2020-10-02	-4.64	12
IFG-14		2020-10-02	2020-10-14	18.13	12
IFG-15		2020-10-14	2020-10-26	-49.36	12
IFG-16	**59 ASCENDING**	2020-07-27	2020-08-02	69.64	6
IFG-17		2020-08-02	2020-08-08	-75.10	6
IFG-18		2020-08-08	2020-08-14	-8.86	6
IFG-19		2020-08-14	2020-08-20	175.97	6
IFG-20		2020-08-20	2020-08-26	-226.75	6
IFG-21	**161 DESCENDING**	2020-07-22	2020-07-28	-169.19	6
IFG-22		2020-07-28	2020-08-09	30.39	12
IFG-23		2020-07-28	2020-08-03	99.88	6
IFG-24		2020-08-03	2020-08-09	-70.12	6
IFG-25		2020-08-09	2020-08-15	2.14	6
IFG-26		2020-08-15	2020-08-21	121.22	6
IFG-27		2020-08-21	2020-08-27	-196.82	6

Bt: temporal baseline; **Bp**: perpendicular baseline.

The ~~All~~ temporal baselines ~~time interval~~ for all InSAR pairs ~~processing is~~are 6 days, except the last three pairs of the ~~66~~ ascending ~~pass~~ orbit 66 that have 12 days. Furthermore, since a bad coherence map of the IFG-24 (Orbit 161), may lead to misinterpretation of results, ~~early~~ prior acquisition ~~images~~ data (before the 3rd of August) ~~with a time interval of 12 days are~~ is selected ~~for~~ to generate the co-event interferogram ~~for the 161 descending pass~~ (IFG-22)~~,~~. ~~t~~Therefore the temporal baseline is 12 days. The gray ~~cells~~ rows in Table 1 represent the co-event interferograms of the three orbits. The perpendicular baselines guarantee~~s~~ also a good quality of InSAR studies (Braun, 2019). As LiCSBAS time series analysis aims to investigate long period displacements and velocities over a large area~~,~~: 34 interferograms ~~IFGs from the~~ from orbit 66 and 190 ~~interferograms~~ interferograms collected ~~IFGs~~ f~~or~~rom the 161 ascending track (Table 2), are selected for the present study.

Table 2. LiCSAR frames, analyzing periods and the total number of IFGs used in this study.

Frame ID	Date		Period	IFGs
	Start	End		
161A_05343_090806	2015-4-26	2020-9-26	66 month	190
066D_05394_131311	2020-4-5	2020-9-26	6 months	34

Table 2bis. Sentinel-2 optical images collected for the study case.

Frame ID	Date	Duration days, to the main shock
Image 1	2020-07-30	-7 days
Image 2	2020-08-09	+ 2 days

3 Methodology description and results

Four aspects are investigated and compared in the present case study:

- The SAR Interferometric (InSAR) methodology, which is subdivided into three sub-groups:
    - DInSAR for the phase changes (fringes),
    - CDD for the coherence change detection,
    - Time series analysis and LiCSAR data.
- The optical image processing.

~~For the results section, e~~Every image contains the description of its source, ~~by~~i.e. IFG-ID (Tables 1, 2, and 2bis) or ~~by~~ the image's acquisitions dates.

3.1 SAR Interferometric methodology

The ~~Interferometric~~ Synthetic Aperture Radar (~~In~~SAR) is an active microwave imaging system. It is independent of sunlight and ~~can~~ penetrates clouds, unlike ~~optical imaging systems which are passive~~passive optical imaging systems. The interferometric ~~In~~SAR method uses the phase components of co-registered SAR images of the same pixel to estimate the topography and to measure the surface change in the target area (Kim, 2013). At least two constellation images are needed to generate an interferogram, which contains topographic, atmospheric effect, baseline error, and noise components (Goudarzi, 2010; Kim, 2013; Netzband et al., 2007):

$$\phi = \phi_{disp} + \phi_{flat} + \phi_{topo} + \phi_{atm} + \phi_{orbit} + \phi_{noise} \quad (1)$$

Where ϕ_{disp} is the line-of-sight (LOS) displacement,~~-~~ ϕ_{flat} the flat earth phase,~~-~~ ϕ_{topo} the topographic phase, ϕ_{atm} is an atmospheric phase, ϕ_{orbit} , the baseline phase and ϕ_{noise} is noise phase contribution (Kim, 2013).

The main steps ~~for the study~~of processing~~, by~~ data using SNAP software (DInSAR and CCD)~~,~~ are depicted in Fig. ~~3~~4. It's worth notice that for CCD processing, it is not necessary to follow the whole (DInSAR, Phase Unwrapping, and Phase to displacement).

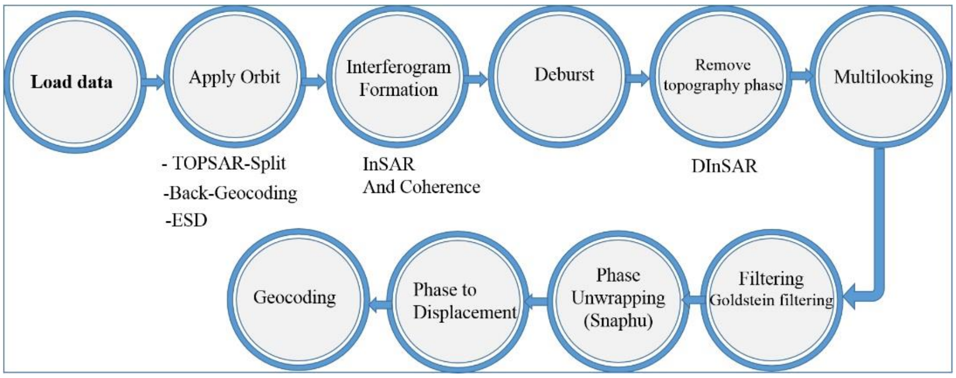

Figure ~~3~~4. Workflow chart for the DInSAR processing using (SNAP) software.

3.1.1 Differential radar interferometry (DInSAR)

Differential radar interferometry (DInSAR) exploits the phase difference to measure coherent changes or deformation between two image acquisitions. It is often used for ground subsidence measurement (Canaslan Çomut et al., 2020; Galve et al., 2015). One of DInSAR's limitations is that the changes are not measurable in the case of non-coherent events (e.g., rapid landslide) (Braun, 2019) ~~which~~such as ~~is~~ the ~~case in this~~present study.

3.1.2 Coherence Change Detection (CCD) ~~Times series analyses~~

The estimated coherence is considered as a quality indicator of an interferogram (Jacquemart and Tiampo, 2021). Actually, it indicates that the phase and amplitude of the received signal express the degree of similarity between the images pair. The pixel coherence γ of two SAR images is estimated on the basis of N neighboring pixels (Jia et al., 2019; Wang et al., 2018).

$$\gamma = \frac{\sum_{i=1}^{N} S_{1i} S_{2i}^{*}}{\sqrt{\sum_{i=1}^{N} |S_{1i}|^2 \sum_{i=1}^{N} |S_{2i}|^2}} \quad (2)$$

Where: S_{1i}, S_{2i}, are the complex signal values of the SAR image pair, N is the window of neighboring pixels, $*$ is the complex conjugate.

The coherence values range between 0 and 1 so that the map is represented as a gray color which 0 is white and 1 is black.

3.1.3 Time series analysis and LiCSAR data

The "*Looking into Continents from Space with Synthetic Aperture Radar*" (LiCSAR) ~~LiCSAR~~ system processes automatically Sentinel-1 ~~InSAR~~ datasets for InSAR use, and generates wrapped, unwrapped interferograms and coherence maps (Lazeckỳ et al., 2020b), with a final product resolution of ~26.5 m (Lazeckỳ et al., 2020a). For such purposes, the open-source LiCSBAS software, adopted in the present study, is used for InSAR time series analysis based on LiCSAR data. It ~~is able to~~can generate maps of ~~mean~~ LOS displacement velocity ~~displacement~~ and deformation time series for all processed frames. Furthermore, it is easy to implement and does not request high-performance computing facilities (Morishita, 2021).

In addition, the mechanism of landslides can be thoroughly studied through LiCSBAS analyses. They rely on the ~~the~~ InSAR time-series analysis package integrated with ~~Looking into Continents from Space with Synthetic Aperture Radar (~~LiCSAR~~)~~, (Lazeckỳ et al., 2020b). Such ~~time~~ time-series analyses are very ~~helpful~~ useful in identifying, for a given landslide or ~~geological~~ ground ~~disorder~~deformations and displacements, the prior patterns of ground movements versus the time ~~as well as foreseeing a potential disorder~~hazards.

3.2 Optical image processing

The optical ~~methods~~ sensors are ~~a~~ passive detection ~~methods~~means ~~way~~ that need~~s~~ sunlight and clear weather conditions ~~in order~~ to exploit the data. The Sentinel-2 is a multi-spectral instrument (MSI) that measures reflected solar radiance in 13 bands with a spatial moderate-resolution of 10 m in the red, green, blue, and near-infrared bands (Laneve et al., 2021).

~~-~~The optical data collected from the ESA platform (Sentinel-2) is treated and plotted using QGIS software to generate true color images (bands 2, 3, and 4 corresponding to RGB)~~, in the present study~~. ~~We skipped~~The present study skips the image of 3rd, Aug 2020 due to bad weather conditions, so that only the two images collected and mentioned in the table 2bis ~~above~~ were used to validate the ground changes detected by InSAR.~~.~~

4 Application to the case study and results

The case studies are located in two different sites and both areas of interest are located in Algeria. They have a hilly relief: the first one is located northeast of Mila City (Grarem) and the second is at the west part of Mila City (Kherba). To monitor the AoIs, several ~~available~~ images are processed and used with different orbits directions (~~Ascending and Descending~~total of 35 ascending and descending acquisitions, see Fig. 1), ~~in order~~ to catch deformation from different angles along the sensor's LOS. The InSAR technique is used in both areas, ~~in order~~ to detect land deformation and landslides ~~caused~~triggered by the earthquake.

~~The present study uses Sentinel-1 A and B datasets: The Sentinel-1 sensors have a wavelength of 5.546 cm (ESA) and are right side-looking with an incidence angle ranging approximately from 20° to 46° (ESA, 2012), which are suitable for change detection and the monitoring of large areas. Furthermore, optical sensors data from Sentinel-2 are used in order to validate the ground changes detected by InSAR.~~

The ~~four~~ adopted methods are applied for Mila case study ~~in order~~ to:

- detect and measure the co-event surface displacements and landslides, caused by the earthquake (CCD and DInSAR)
- monitor their dynamic evolution in the first weeks and months, at the post-event period (CCD and LiCSAR data).

- analyze their possible initiation ahead of the earthquake by months and years, at the pre-event period (Time-series methods and LiCSAR data).
- corroborate the results by comparing several methods outputs, i.e. SAR (CCD, DInSAR, LiCSAR), aerial optical photo (Sentinel-2), and field surveys.

The quality of the SAR image is consistent with the topography slopes and area roughness. Actually, the AoI has rough topography, hills, and rivers (Fig. 2). Selecting either ascending or descending passes, relying on which will avoid some limitation of InSAR is an extremely essential action ~~able~~ to infer the deformation from various angles. Therefore, considering the regional topography and geology of the AoI is necessary to process InSAR and results interpreting.

~~(a) (b) (c)~~

~~**Figure 4.** 3D view of AoIs, Kherba AoI and Grarem using QGIS with DEM SRTM 1sec and ESRI basemap, a & b are Kherba AoI, c is the Grarem case area, the red polygon is the boundary of change detected by InSAR.~~

Differential InSAR (DInSAR) method is helpful to investigate co-seismic effects and detect ground changes ~~in the ground~~. The produced Interferograms and coherence images are projected to WGS84 reference, with a pixel size of 13.4 m. The unwrapped interferograms ~~below~~ present phase contribution of many noise resources (atmospheric), see Fig. 5. In general, strong earthquakes cause large-scale fringes patterns around the epicenter which is not the case in the event under study (a moderate earthquake). Processing DInSAR analysis may then lead to misinterpretation due to atmospheric contribution in differential phase interferograms (Fig. 5). In the study case, no regional deformation due to the earthquake is observed and there is no need to continue investigating the dam and the two bridges by simple DInSAR. However, to monitor the dam and bridges, it is highly recommended to use PS-InSAR for regional and local ground deformation detection (Hooper et al., 2004; Rapant et al., 2020; Sanabria et al., 2014).

~~this moderate earthquake has triggered small deformation and landslides in Grarem, Kherba, and Azeba, see Figs. 7, 10, and 20.~~

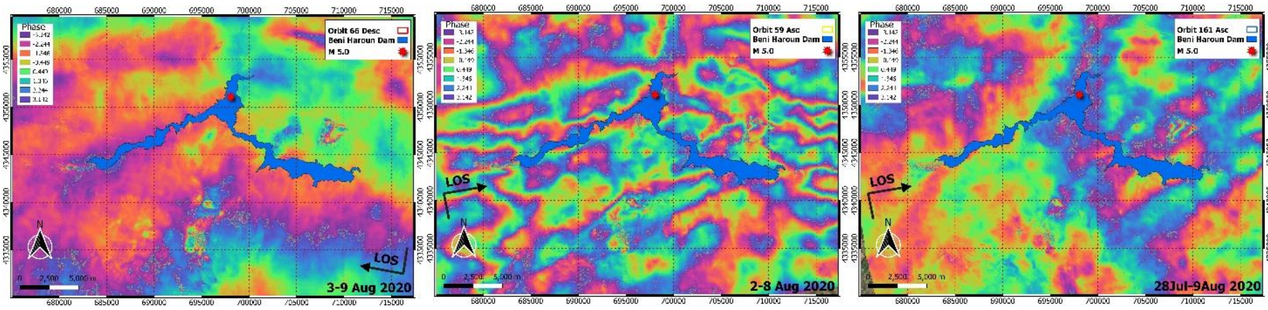

Figure 5. Wrapped Interferograms from Sentinel-1 for IFG-3+IFG-4, IFG-17 and IFG-22, The red star is the epicenter location (USGS).

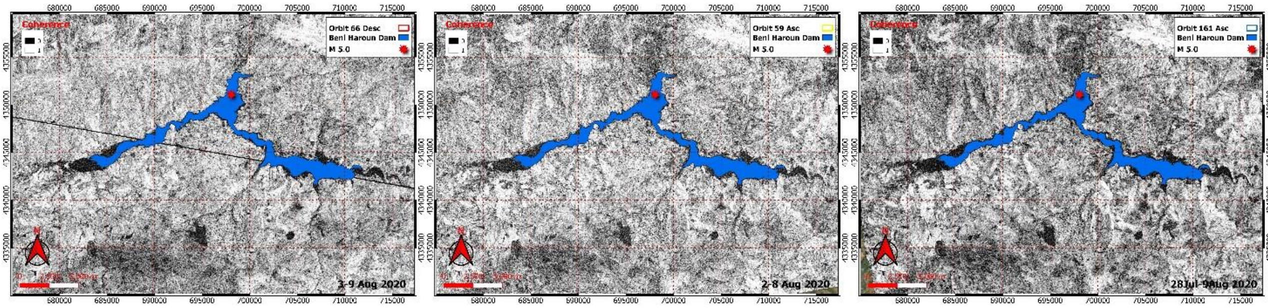

Figure 6. Mila Area, InSAR coherence maps for IFG-3+IFG-4, IFG-17 and IFG-22.

~~t~~This moderate earthquake has triggered small deformation and landslides in Grarem, Kherba, and Azeba~~, see Figs. 7, 10, and 20~~.

The IFG-3 and IFG-4 are merged in one image due to the AoIs (Kherba and Grarem), which are located ~~between~~ in two different image acquisitions ~~in~~ of the descending orbit number 66. ~~In order to monitor the dam and bridges, it is highly recommended to use PS-InSAR for regional and local ground deformation detection .~~

4.1 Case of GRAREM

The detection of deformation or changes between two InSAR images reveals a small change in the region of Grarem. This change is ~~detected~~ observed as small fringes, each fringe corresponding to a displacement of a half-wavelength (λ=5.546 cm) in the LOS direction (Fig. 7). Usually, coherent change does not appear in coherence images as dark region, but in the study case, the outer borderline of the fringes region shows incoherence change which is clearly visible in coherence maps (Fig. 8).

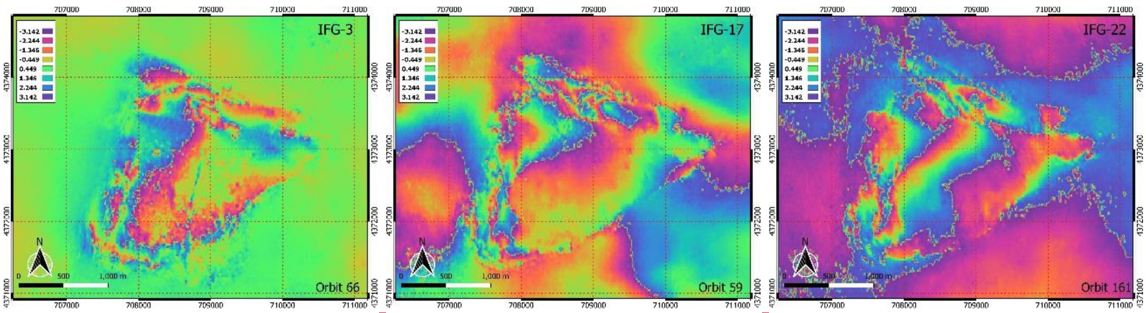

Figure 7. Detected fringes in Interferograms N° 3, 17, and 22, focused images on Grarem zone.

A ~~time~~ time-series analysis needs then to be performed out to prove whether this contour was formed at the event occurrence date (August 7, 2020). The coherence maps of the co-event period present a dark polygon ~~which~~ that is related to incoherent change or deformation. But inside the AoI, the results show ~~a~~ some coherent changes which mean~~s~~ that this area has deformed as a block up or down.

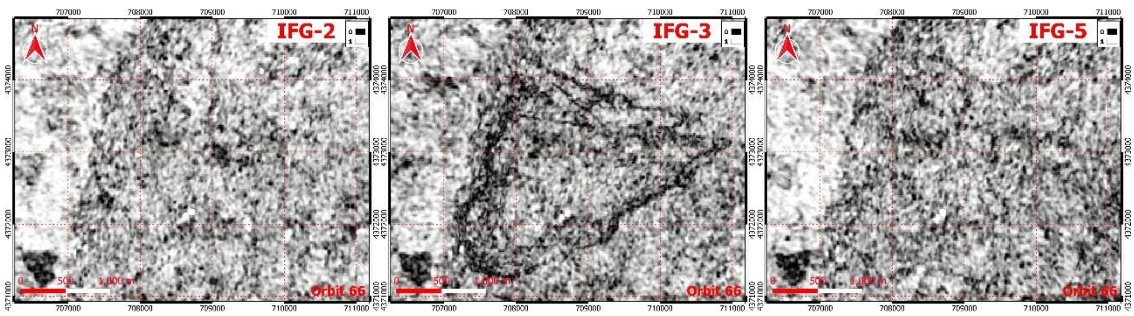

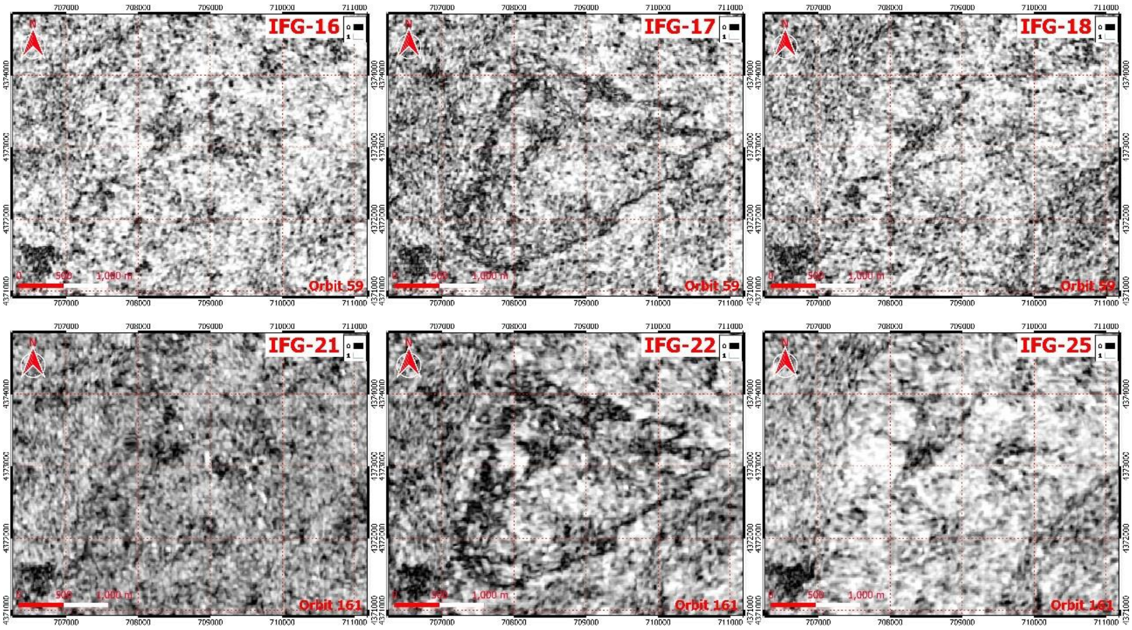

Figure 8. Coherence maps of Grarem AoI: the images represent pre-event (left), co-event (middle), and post-event (right) for ~~each~~ orbits 66, 59, and 161. *Nota:* ~~,~~ *the co-event maps for the three orbits show the decay of coherence that is triggered by the earthquake*.

According to phase and coherence maps, ~~The~~ the affected area is approximately ~~covers about~~ 3.94 km^2 ~~as estimated from phase and coherence maps~~, with an average runout distance of 2.6 km from ~~the~~ top to downhill ~~of 2.6 km~~ (Fig. 2.a distance from point 1 to point 2).

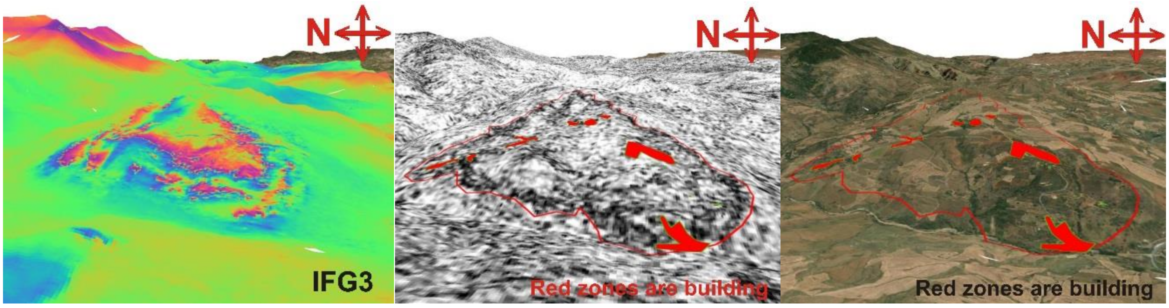

Figure 9. 3D view of Grarem Area, Images of IFG-3. Each fringe = wavelength/2 in LOS, and red zones represent existing building compounds (QGIS, ESRI basemap).

4.2 Case of Kherba

DInSAR has abundantly demonstrated its reliability as a technique for monitoring slow movements ~~is expected to be more suitable for slow and gradual movements~~ (Cascini et al., 2013; Wempen, 2020). In the present study, Kherba's landslides exceed the capabilities of DInSAR since this method cannot measure the ~~changes~~ deformations due to incoherent change at the first event. Phase images of the Region of Interest (RoI) show a clear decorrelation and consequently, the phase information is no longer convenient for analysis.

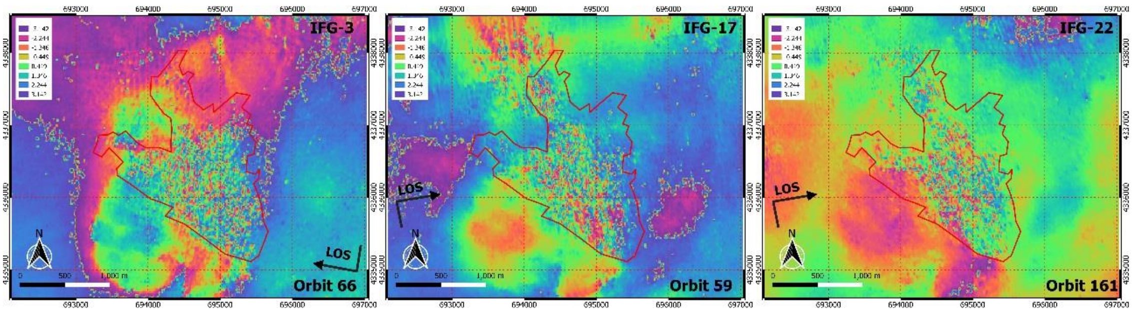

Figure 10. Kherba main event interferograms, biased pixels ~~in~~ inside the ~~RoI~~ red line correspond to incoherent changes.

In such cases of incoherent changes in the scene, DInSAR is useless whereas ~~we can serve to~~ the Coherence Change Detection ~~coherence change detection~~ (CCD) method ~~which is~~remains useful and suitable ~~and able~~ to monitor the event.

4.2.1 CCD Times series analyses

For the case study, the coherence maps (Figs. 11-13) show very low coherence in the Kherba area ~~(RoI) and~~, indicat~~e~~ing that some changes have occurred. ~~This may confirm whether the decrease of coherence values is due to the hazard or it is naturally low.~~ The ~~Coherence Change Detection (~~CCD~~)~~ ~~is useful when the change is incoherent in the scene, since CCD~~ quantifies changes between two SAR images~~,~~ and ~~is~~ is represented as a ~~a~~ decay of coherence values (co-event maps). ~~This may confirm whether the d~~Decreases ~~of~~in coherence values can be caused by a variety of factors such as ~~earthquake,~~ geotechnical landslides as well as ~~including~~~~is due to the hazards or it is~~~~being naturally low (e.g., water~~water, vegetation…). ~~–~~ To distinguish between natural low coherence ~~(e.g., water, vegetation…)~~ and induced surface changes, a second coherence map (pre-event or post-event) is ~~needed~~ required ~~in order~~ to serve as a ~~reference~~ reference~~and to~~, which can be compared with the main ~~pre~~co-event images. It is preferable to mask out the rest of the non-changed area using~~with~~ a ~~ratio of~~ pre-event ~~by~~to co-event image ratio and filter values ~~that are~~ equal to or~~f~~ less than 1 (see Fig. 13).

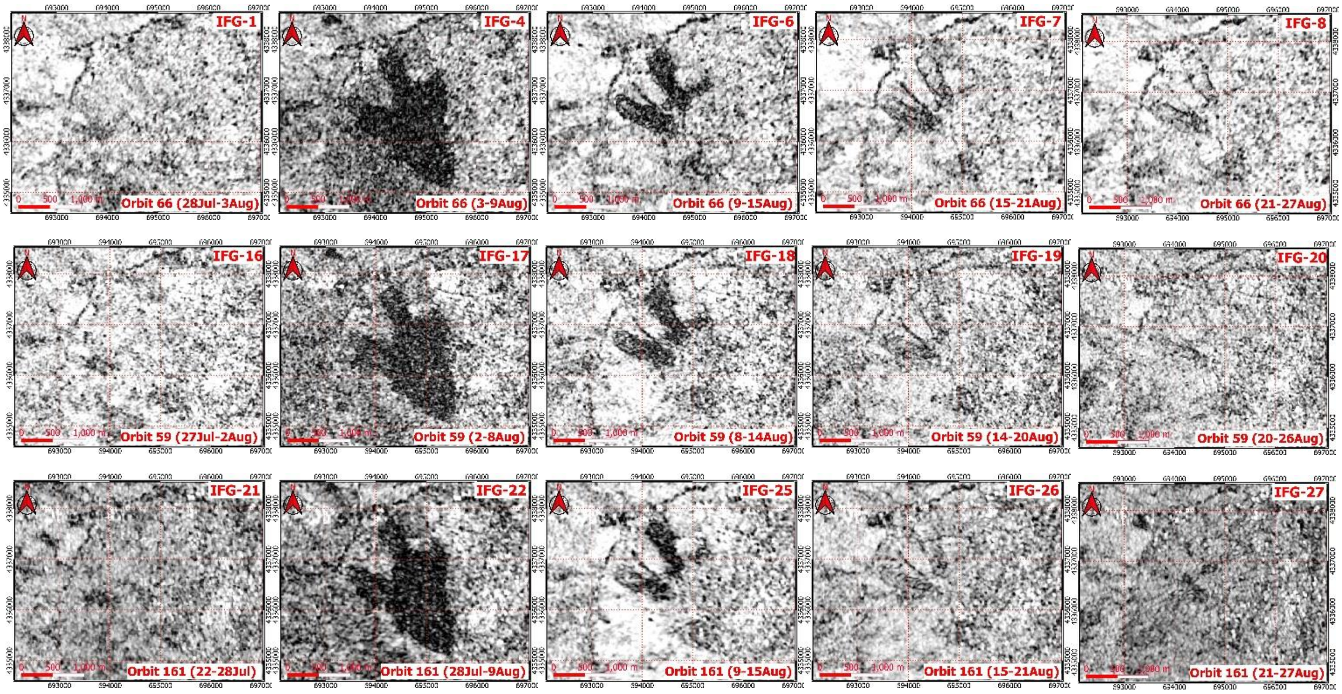

Figure 11. Coherence time series maps of the Kherba landslide, Sentinel-1.

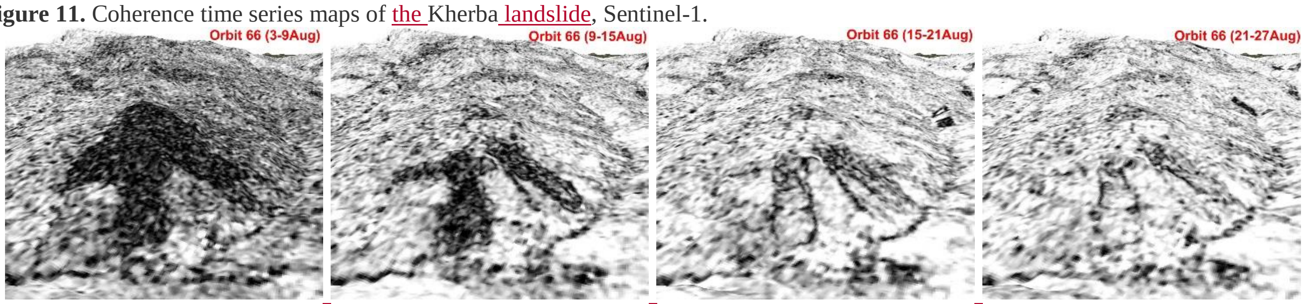

Figure 12. 3D view of Kherba ~~City~~landslide, Sentinel-1 Coherence images of ~~-~~Orbit 66 with a 6-day temporal baseline, the dark areas are the landslide and deformations zones.

The CCD time-series analysis displays the changes in the AoI over time for the Kherba landslide. The dark region represents the main changes that occurred during the co-event period (earthquake date). The landslide shape is divided into two toes at the lower side of the Hill, as shown in Figs. 11 and 12.

During the first week following the earthquake, changes are detected in the lower side of the hill~~,~~ and lasted until the late date of August 2020 (IFG-8 orbits 66, IFG-27 orbit161, and IFG-20 for orbit 59). Afterwards, many other sources of noise were present in the AoI, which makes this technique less efficient (weather, human activities). Most of the processed images are 6 days' intervals, except the orbit 161 in which the co-event ~~image~~ interferogram (IFG-24) was not good enough ~~good~~ (bad coherence) to compare with other pre-~~post~~ post-event images~~:~~, ~~it is then~~so it was replaced by the IFG-22. Figures~~s.~~ 14 and 15 illustrate how the ~~image~~ interferograms selection may change the interpretation of results.

To quantify the change, an RoI ~~is~~ represented in Fig. 13 (green rectangle) is selected for analysis~~,~~. ~~and the~~ The plots in Figs. 14 and 15 show~~s~~ also the frequency distributions of coherence values within the RoI. Table 3 displays the calculated average coherence values of the RoI and the ~~decreased~~ percentage ~~values inside the RoI~~of changes. For the ~~66~~ orbit~~'s~~ 66 pairs, the RoI average coherence starts by 0.66 during the pre-event period (IFG-2) and decreases to 0.51 during the co-event period (-~~31~~23%) (IFG-3). For orbit 59 pairs, it decreases by ~~27~~22% after an initial mean value of 0.77 (IFG-16)~~with~~ and a mean value of 0.60 (IFG-17)~~after an initial mean value of 0.77 (IFG-16)~~.

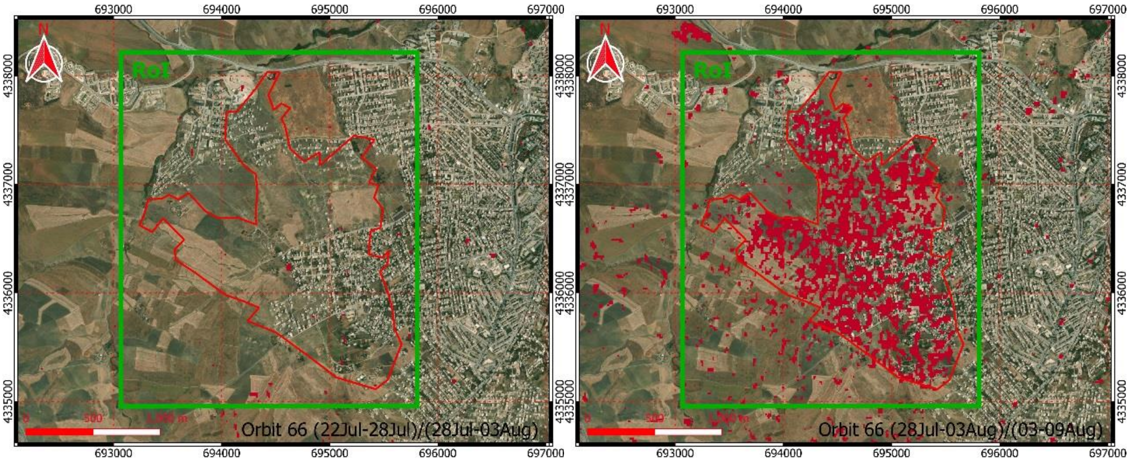

Figure 13. Pre-event coherences ratio (left), co-event coherences ratio (right), Sentinel-1 Orbit 66. The green box indicates the scope of the RoI, red spots represent significant changes of coherence in the landslide region (QGIS, ESRI World Imagery basemap).

The last orbit 161 pairs make an exception due to ~~an~~ the initial bad coherence maps (IFG-23 and 24), as shown in Fig. 15, where the dotted green line has low coherence compared to the co-event coherence map (red dotted line). So, the orbit 161 acquisition of the 3rd August must be skipped and not used for the analysis~~and the interpretation~~. ~~And i~~It was replaced by the previous acquisition ~~of~~on July- 28th. ~~see Fig. 14.c.~~ However, the previous pair (IFG-21 and IFG-22) ~~gave~~ had a value of 0.57 (IFG-21) ~~which~~ that decreased to 0.52 (IFG-22), representing a 9 percent~~i.e. 11%~~ of change.

Table 3. Mean coherence change values inside the ROI.

Orbit	Pre-event coherence mean	Co-event coherence mean	Post-event coherence mean	Pre-event Change	Post-event Change
66	28Jul_03Aug	03_09Aug	09_15Aug	-~~31~~23%	+24%
	0.66	0.51	0.63		
59	27Jul_02Aug	02_08Aug	08_14Aug	-~~27~~22%	+15%
	0.77	0.60	0.69		
161	22Jul_28Jul	28Jul_09Aug	09Aug _15Aug	-~~11~~9%	+37%
	0.57	0.52	0.71		

The lines in Figure 14 indicate the frequency distributions of coherence time series maps. The green line in Fig.14.a represents the pre-event coherence distribution, while the red line represents the post-event coherence distribution, which clearly shows a decay of the mean coherence after the main event (dates and values are presented in the legend).

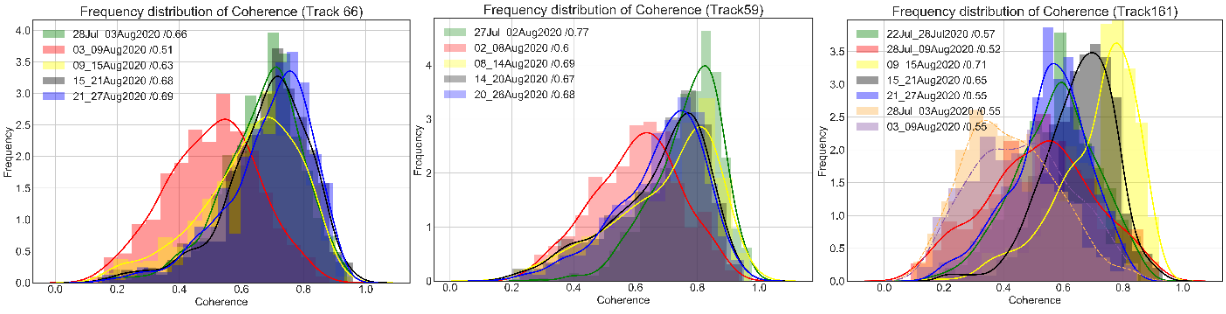

(a) **(b)** **(c)**

Figure 14. Frequency distributions of coherence values within RoI for all coherence time series images.

Figure 15 illustrates why ~~we chose~~ the interferogram of the 22-28July (green line) is chosen as the pre-event (initial) even though there is another IFG of (28July-3Aug green dotted line) ~~with~~i.e. only four days before the main event (7 August 2020).

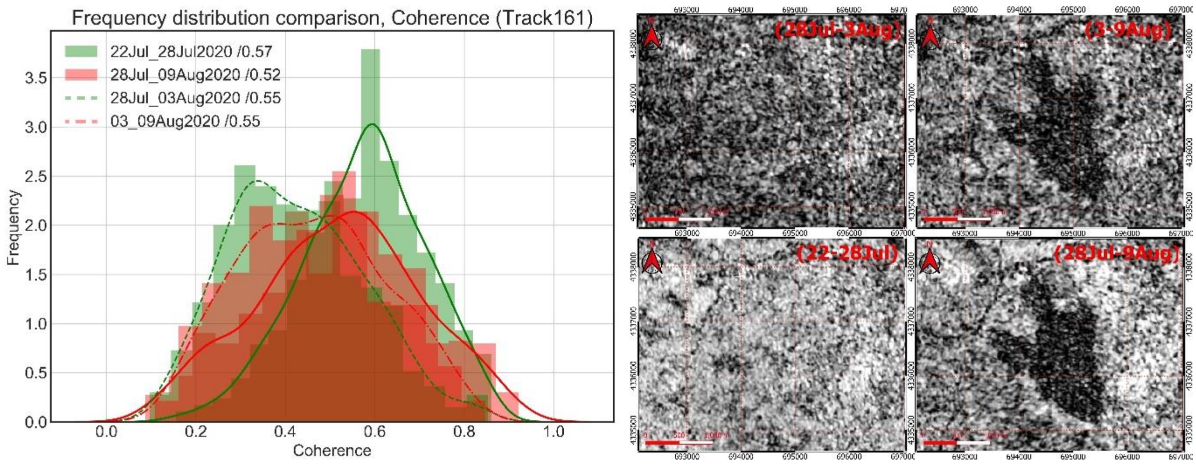

Figure 15. Effect of bad coherence ~~shift~~: the cause is the acquisition of 3rd August start at (17:28:15, orbit 161) under bad weather conditions in the acquisition time according to precipitation site (WWO) (rainfall in that daytime), compared to the acquisition of the same day but not the same time (05:37:58 for orbit 66).

The surface area derived from the coherence images covers 2.1 km^2, ~~derived from the coherence images,~~ and the shape ends by two toes. The runout distance is 2.4 km for the right toe and 2.15 km for the left one. The CCD method has the potential to differentiate between the areas impacted by induced changes and those affected by other sources of noise. The ratio operation is useful in canceling out other noise factors and improving~~e~~ the detection of changes in the region.

4.2.2 Optical detection

To validate the SAR methods results, two images from Sentinel-2 are downloaded and treated using QGIS software, the dates of the images ~~being dated~~are 2020-07-30 (a week before the main shock), and 2020-08-09 (two days after the main shock)~~, and the optical data is treated using QGIS~~.

- The optical ~~passive~~ detection shows that an important ~~ground surface~~ displacement affected the ground ~~of~~in the Kherba neighborhood, over an area of 1.32 km^2. The landslide shape of deformation has only one toe at the lower part of the hill (blue line Fig. 16.b) compared to the CCD method results.

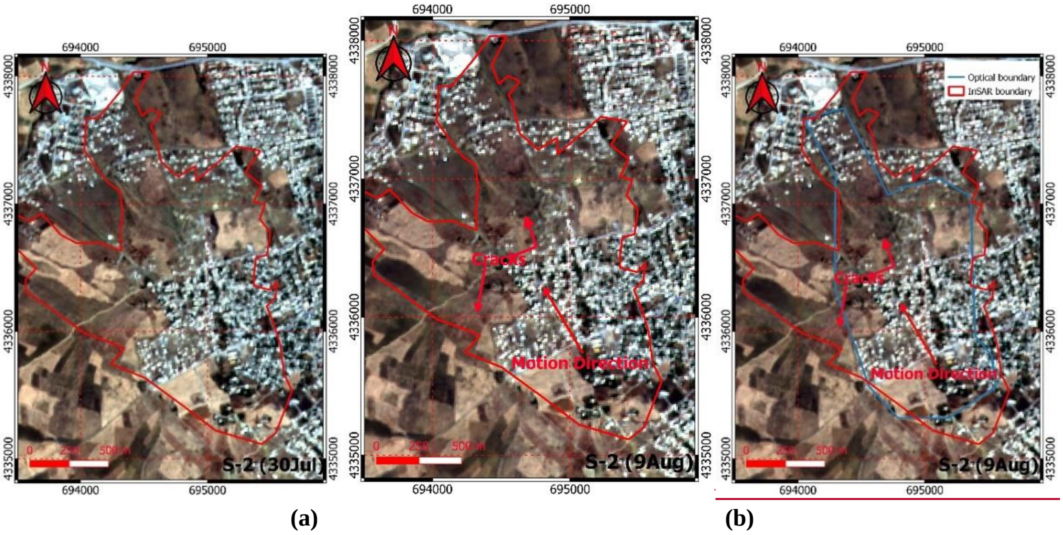

Figure 16. Sentinel-2 Optic Images: (a)- dated 30-Jul 2020, (b)- dated 09-Aug 2020.

- The optical images were unable to detect the ~~disorders~~ground deformations and displacements -in Grarem in which there was no apparent landslide although there were a lot of ruptures and cracks. However, a field inspection has confirmed the results of the CCD and DInSAR analysis in terms of pattern and limits of the zone affected by the deformation (surface rupture).

4.3 LiCSBAS analyses

~~LiCSBAS is an open-source program for InSAR time series analysis based on LiCSAR data. The LiCSAR system automatically processes Sentinel-1 InSAR datasets (Lazeckỳ et al., 2020b), to generate wrapped, unwrapped interferograms and coherence maps (Lazeckỳ et al., 2020b), with a final product resolution of ~26.5 m (Lazeckỳ et al., 2020a). LiCSBAS exploits the data of LiCSAR in order to generate maps of displacement mean velocity and deformation time series plots (Morishita, 2021).~~

Displacement time series and velocities analysis of the region is performed out using LiCSBAS that exploits the data of the LiCSAR system (Morishita, 2021). It allows identifying whether unstable conditions pre-existed or are still undergoing. The study started from the 5th of April to the 26th of September 2020, for the orbit 66 and from 26 April 2015 to 26 September 2020 for the orbit N° 161.

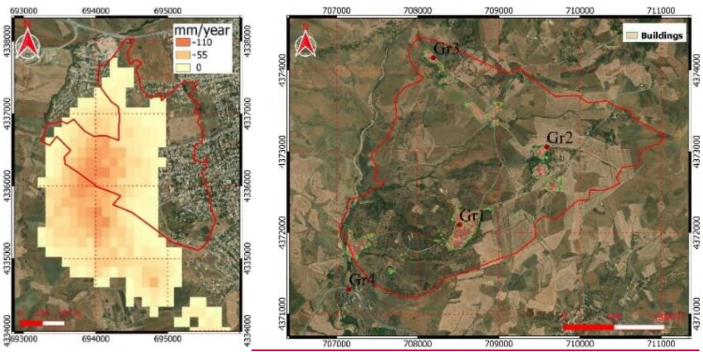

Figure 17. (a) Line of sight ~~(LOS)~~ displacement velocity map, the red line is landslide area (066D_05394_131311), (b) Grarem case selected points for time-series analysis, (QGIS, ESRI basemap).

The ~~time~~ time-series analysis detected subsidence ~~at~~ of the west part of Kherba. This region is on the other hillside of Kherba Hill, and both sides have a significant slope. A site investigation did not find any drilled wells. One may assume that this subsidence is not caused ~~due to any~~by the pumping of groundwater. Therefore, another possible explanation is probably related to the large mass movement of the main landslide hillside (red polygon), causing the opposite side of the hill to move down (subsidence). The displacement velocity in Kherba is about 110 mm/year, Fig. 17.

For the Grarem case, the velocity map looks stable between the same dates (April 5 to September 26, ~~2021~~2020). The change occurred rapidly and is removed by the filters. For illustrative purposes, the displacement time series of some points are illustrated in Figs. 18 and 19.

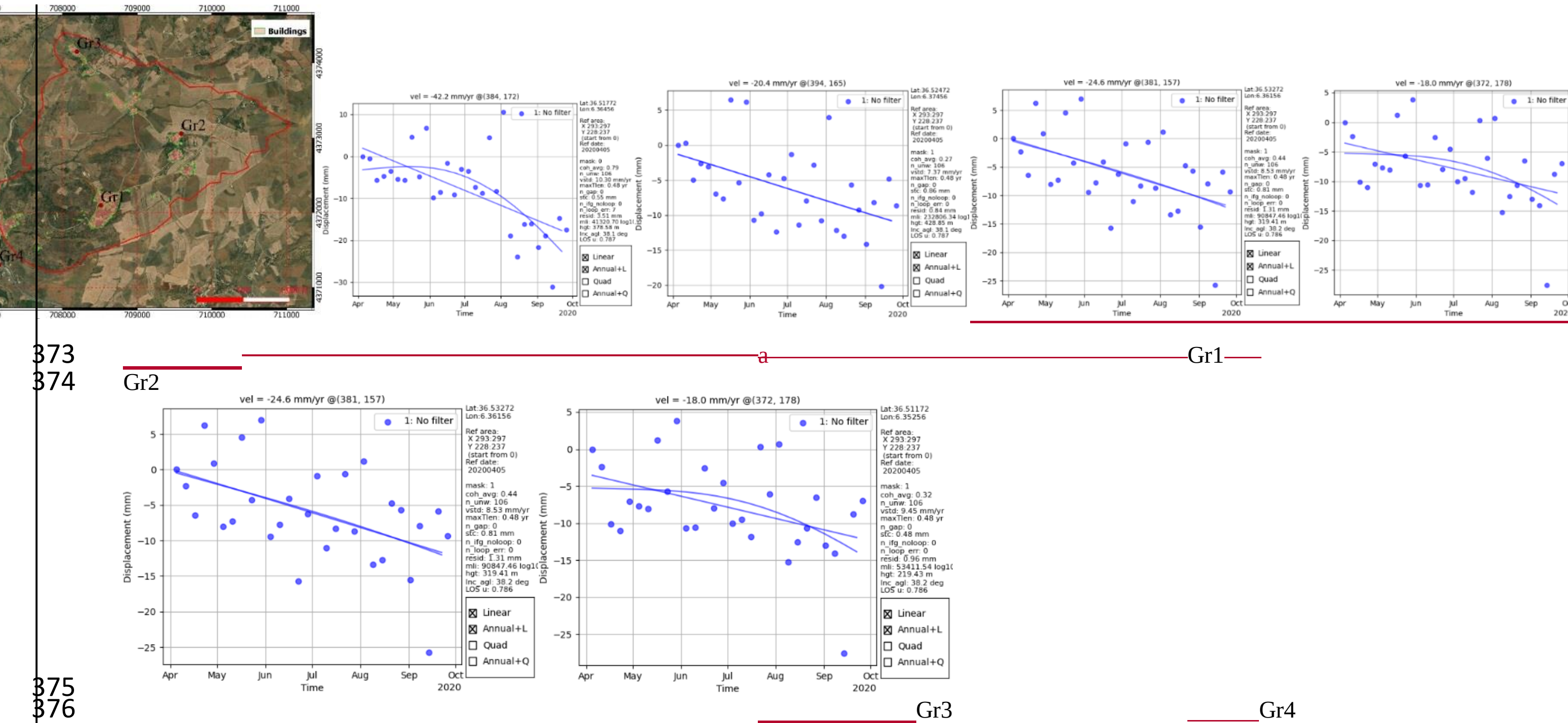

Figure 18. Displacement time series (orbit 66, ~~)~~Grarem case), corresponding to the points in image (~~a~~17.b), the displacement is relative to ~~the~~ a reference point~~, (a) Grarem region~~, the plots present~~s~~ a great dispersion of data points which is related to many noise resources (weather, man-made, etc.), and short period of analysis, (QGIS, ESRI basemap).

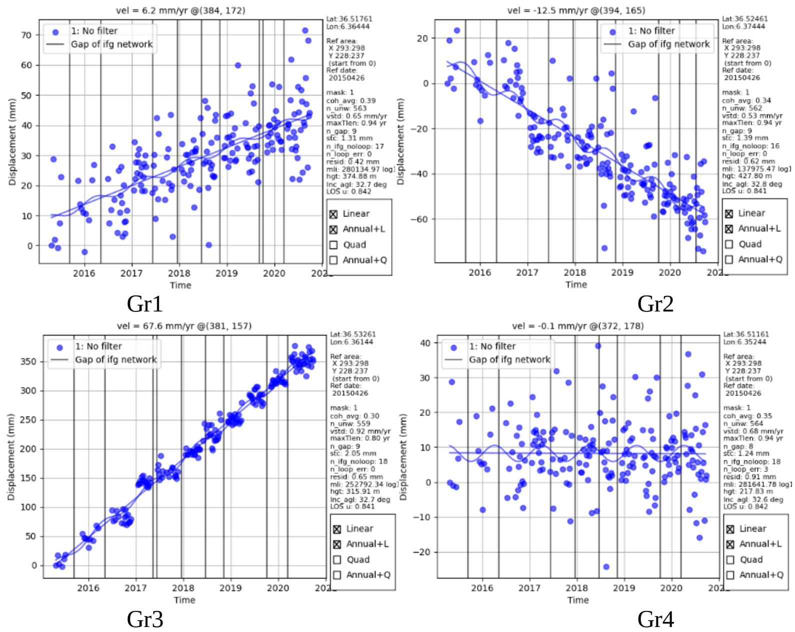

Figure 19. Displacement time series (orbit 161), corresponding to the points in Fig. 1~~8~~7.~~a~~b~~, displacement is relative to the reference point~~ The plots show less dispersion of data points (linear) compared to short analysis, the long period analysis (5 years) is useful to eliminate other sources of noise.~~.~~

During the LiCSBAS processing, a primary stable reference point is selected at (36.455885° N, 6.276909° E). This method proves to be efficient for large-scale deformation monitoring and slow coherent changes, long time series analysis is useful in reducing other noise factors.

4.4 Discussion

InSAR monitoring proves its ability to detect land changes. First, landslides and land deformation can be detected remotely by InSAR. Furthermore, optical images could detect only one case (Kherba). The theoretical results were validated by site visiting and investigation, i.e.:

- Compared to results obtained from optical for the Kherba landslide, InSAR is more precise for detecting small deformation (2 toes in CCD maps). Besides, the ~~other~~ optical ~~techniques~~ ~~way~~analysis did not detect the full deformed ~~changing~~ area in the region (only one toe).
- Large-scale ~~L~~landslides ~~of this magnitude~~ exceed DInSAR's ~~the~~ capabilities ~~of DInSAR~~, ~~and their~~which induce an extreme loss of coherence. The ~~-~~co-event interferograms ~~of co-events~~ are strongly decorrelated. Therefore, the phase information is no longer usable and one cannot measure the displacement of incoherent ground changes (Landslide).
- Land deformation in Grarem first detected by DInSAR, was confirmed by a site visit, during which small cracks were visible on the ground (incoherent boundary region). Due to incoherent boundaries and because the displacement is probably larger than what can be measured by one ~~interferogram~~ fringe cycle (depending on the wavelength, 5 cm for Sentinel-1), the deformation measurements in this case are not reliable and accurate.
- Another landslide detected by InSAR in the Azeba region (6 km east of Mila) was visited too: the area covers 0.42 km^2 and the site investigation ~~(Fig. 20)~~ confirms the landslide (Fig. 20).
- Analysis with LiCSBAS revealed new hillside deformation (subsidence) which is probably a consequence of the mass that moved in the main landslide hillside. Displacements time series, ~~in~~ of the Grarem region at some points, show deformation along LOS with velocities ranging from 6 mm/year to 67 mm/year. This method is preferable in ~~the~~ large-scale area and ~~large~~long-period analysis.

(a) **(b)** **(c)**

Figure 20. Landslide occurred in Azeba region (2 km North) detected by InSAR: *(a) & (b)- visible ground cracks, (c)- coherence map of Azeba zone delimited by the cracks*.

5 Conclusions and Recommendations

In this paper, active and passive space-based satellite data are used to monitor and study the impact of natural hazards (earthquakes and landslides) on struck areas. The C-band Sentinel-1 SAR datasets (active sensing) and optical images of Sentinel-2 data (10 m spatial resolution) were used in this study to investigate the area, the passive images were used only to validate the active sensing results. For the InSAR processing, the use of DInSAR, CCD methods, and the LiCSBAS tools ~~has~~ have been able to generate a detailed time series analysis of ground changes.

InSAR techniques have proved their ~~efficacy~~ efficiency ~~can~~ to extract useful geodetic information, such as the ground movement and track surface deformation over large areas with centimetric accuracy in coherent change cases. The present research study has demonstrated that the InSAR processing is adapted to study earthquake and landslides zones. As a result, three primary land failures were detected over the study area using InSAR.

DInSAR is poorly suited to track and detect~~ed~~ landslides. It is represented as a pixel decorrelation in phase interferograms and high decay in coherence values. CCD is further suitable to map earthquake-induced landslides that may remain undetected using coherent methods (DInSAR). The estimation of their horizontal/vertical displacements is a challenge to be inferred.

The Grarem deformation looks like~~as~~ a landslide that has just been initiated~~,~~ but might extend under an upcoming triggering event. Actually, the failure plane rim is presented as a dark line in the coherence map or as the fringe circumference ~~of the fringe~~ in phase maps (estimated area 3.94 sq. km). This impending land failure needs therefore a thorough and real-time monitoring by the ~~and adequate geotechnical studies.~~ PS-InSAR method, which can ~~serve as an~~provide efficient and low-cost monitoring method able to obtain millimeter-level precision displacement measurements over selected points in the area ~~(Jia et al., 2019).~~(Jia et al., 2019), and adequate geotechnical studies.

It is worth ~~to increase~~increasing awareness of possible future geotechnical threats in a timely manner, through on-site monitoring using GPS, crack meters, and by placing inclinometers in the Grarem area, in order to develop a model of the slope stability.

Acknowledgments: In this work, we used SNAP and QGIS to analyze and plot maps. ~~ESA, Copernicus, and COMET for providing Sentinel data.~~ The authors are grateful to European Space Agency (ESA) for providing freely the data through Copernicus Program and COMET.

Conflicts of Interest: The authors declare no conflict of interest.

References

ASF DAAC: Alaska Satellite Facility, [online] Available from: https://search.asf.alaska.edu/#/ (Accessed 26 June 2021), n.d.

Bakon, M., Perissin, D., Lazecky, M. and Papco, J.: Infrastructure Non-linear Deformation Monitoring Via Satellite Radar Interferometry, Procedia Technol., 16, 294–300, doi:10.1016/j.protcy.2014.10.095, 2014.

Braun, A.: Radar satellite imagery for humanitarian response: Bridging the gap between technology and application, , 225 [online] Available from: https://publikationen.uni-tuebingen.de/xmlui/bitstream/handle/10900/91317/Braun 2019 Radar satellite imagery for humanitarian response UB.pdf?sequence=1, 2019.

Canaslan Çomut, F., Gürboğa, Ş. and Smail, T.: Estimation of co-seismic land deformation due to Mw 7.3 2017 earthquake in Iran (12 November 2017) using Sentinel-1 DInSAR, Bull. Miner. Res. Explor., 162(August), 11–30, doi:10.19111/bulletinofmre.604026, 2020.

Cascini, L., Peduto, D., Pisciotta, G., Arena, L., Ferlisi, S. and Fornaro, G.: The combination of DInSAR and facility damage data for the updating of slow-moving landslide inventory maps at medium scale, Nat. Hazards Earth Syst. Sci., 13(6), 1527–1549, doi:10.5194/nhess-13-1527-2013, 2013.

Congedo, L.: Semi-Automatic Classification Plugin: A Python tool for the download and processing of remote sensing images in QGIS, J. Open Source Softw., 6(64), 3172, doi:10.21105/joss.03172, 2021.

ESA: ESA's radar observatory mission for GMES operational services. [online] Available from: https://sentinel.esa.int/documents/247904/349449/S1_SP-1322_1.pdf, 2012.

ESA: Resolution and Swath - Sentinel-1 - Missions - Sentinel Online - Sentinel, [online] Available from: https://sentinel.esa.int/web/sentinel/missions/sentinel-1/instrument-payload/resolution-swath (Accessed 26 June 2021a), n.d.

ESA: SAR Instrument - Sentinel-1 SAR Technical Guide - Sentinel Online - Sentinel, [online] Available from: https://sentinels.copernicus.eu/web/sentinel/technical-guides/sentinel-1-sar/sar-instrument (Accessed 26 June 2021b), n.d.

Frizon de Lamotte, D., de Lamotte, D. F., Bezar, B. Saint, Bracène, R. and Mercier, E.: The two main steps of the Atlas building and geodynamics of the western Mediterranean, Tectonics, 19(4), 740–761 [online] Available from: https://www.academia.edu/29649745/The_two_main_steps_of_the_Atlas_building_and_geodynamics_of_the_western_Mediterranean (Accessed 6 January 2022), 2000.

Galve, J. P., Castañeda, C. and Gutiérrez, F.: Railway deformation detected by DInSAR over active sinkholes in the Ebro Valley evaporite karst, Spain, Nat. Hazards Earth Syst. Sci., 15(11), 2439–2448, doi:10.5194/nhess-15-2439-2015, 2015.

Goudarzi, M. a: Detection and measurement of land deformations caused by seismic events using InSAR, Sub-pixel correlation, and Inversion techniques, , (January), 127, 2010.

Herrera, G., Fernández, J. A., Tomás, R., Cooksley, G. and Mulas, J.: Advanced interpretation of subsidence in Murcia (SE Spain) using A-DInSAR data - Modelling and validation, Nat. Hazards Earth Syst. Sci., 9(3), 647–661, doi:10.5194/nhess-9-647-2009, 2009.

Hooper, A., Zebker, H., Segall, P. and Kampes, B.: A new method for measuring deformation on volcanoes and other natural terrains using InSAR persistent scatterers, Geophys. Res. Lett., 31(23), 1–5, doi:10.1029/2004GL021737, 2004.

Jacquemart, M. and Tiampo, K.: Leveraging time series analysis of radar coherence and normalized difference vegetation index ratios to characterize pre-failure activity of the Mud Creek landslide, California, Nat. Hazards Earth Syst. Sci., 21(2), 629–642, doi:10.5194/nhess-21-629-2021, 2021.

Jia, H., Zhang, H., Liu, L. and Liu, G.: Landslide deformation monitoring by adaptive distributed scatterer interferometric synthetic aperture radar, Remote Sens., 11(19), 1–18, doi:10.3390/rs11192273, 2019.

Jung, J. and Yun, S. H.: Evaluation of coherent and incoherent landslide detection methods based on synthetic aperture radar for rapid response: A case study for the 2018 Hokkaido landslides, Remote Sens., 12(2), 1–26, doi:10.3390/rs12020265, 2020.

Kim, J. W.: Applications of Synthetic Aperture Radar (SAR)/ SAR Interferometry (InSAR) for Monitoring of Wetland Water Level and Land Subsidence, Ohio State Univ., (503), 1–111, 2013.

Laneve, G., Bruno, M., Mukherjee, A., Messineo, V., Giuseppetti, R., De Pace, R., Magurano, F. and Ugo, E. D. ’: Remote Sensing Detection of Algal Blooms in a Lake Impacted by Petroleum Hydrocarbons, Remote Sens. 2022, Vol. 14, Page 121, 14(1), 121, doi:10.3390/RS14010121, 2021.

Lazeckỳ, M., Hatton, E., González, P. J., Hlaváčová, I., Jiránková, E., Dvořák, F., Šustr, Z. and Martinovič, J.: Displacements monitoring over Czechia by IT4S1 system for automatised interferometric measurements using Sentinel-1 data, Remote Sens., 12(18), 1–21, doi:10.3390/RS12182960, 2020a.

Lazeckỳ, M., Spaans, K., González, P. J., Maghsoudi, Y., Morishita, Y., Albino, F., Elliott, J., Greenall, N., Hatton, E., Hooper, A., Juncu, D., McDougall, A., Walters, R. J., Watson, C. S., Weiss, J. R. and Wright, T. J.: LiCSAR: An automatic InSAR tool for measuring and monitoring tectonic and volcanic activity, Remote Sens., 12(15), doi:10.3390/RS12152430, 2020b.

LNHC: Laboratoire National de l’Habitat et de la Construction, LNHC [online] Available from: http://lnhc-dz.com/ (Accessed 26 June 2021), n.d.

Mazzanti, P., Rocca, A., Bozzano, F., Cossu, R. and Floris, M.: Landslides Forecasting Analysis By Displacement Time Series Derived From Satellite INSAR Data: Preliminary Results, undefined, 2012.

Meng, Q., Confuorto, P., Peng, Y., Raspini, F., Bianchini, S., Han, S., Liu, H. and Casagli, N.: Regional recognition and classification of active loess landslides using two-dimensional deformation derived from sentinel-1 interferometric radar data, Remote Sens., 12(10), doi:10.3390/rs12101541, 2020.

Merghadi, A., Abderrahmane, B. and Tien Bui, D.: Landslide susceptibility assessment at Mila basin (Algeria): A comparative assessment of prediction capability of advanced machine learning methods, ISPRS Int. J. Geo-Information, 7(7), doi:10.3390/ijgi7070268, 2018.

Moretto, S., Bozzano, F. and Mazzanti, P.: The role of satellite insar for landslide forecasting: Limitations and openings, Remote Sens., 13(18), 1–31, doi:10.3390/rs13183735, 2021.

Morishita, Y.: Nationwide urban ground deformation monitoring in Japan using Sentinel-1 LiCSAR products and LiCSBAS, Prog. Earth Planet. Sci., 8(1), doi:10.1186/s40645-020-00402-7, 2021.

Mouloud, H. and Badreddine, S.: Probabilistic seismic hazard assessment in the Constantine region, Northeast of Algeria, Arab. J. Geosci., 10(6), doi:10.1007/s12517-017-2876-5, 2017.

Netzband, M., Stefanov, W. L. and Redman, C.: Applied remote sensing for urban planning, governance and sustainability., 2007.

Pawluszek-Filipiak, K. and Borkowski, A.: Integration of DInSAR and SBAS techniques to determine mining-related deformations using Sentinel-1 data: The case study of rydultowy mine in Poland, Remote Sens., 12(2), doi:10.3390/rs12020242, 2020.

Peláez Montilla, J. A., Hamdache, M. and Casado, C. L.: Seismic hazard in Northern Algeria using spatially smoothed seismicity. Results for peak ground acceleration, Tectonophysics, 372(1–2), 105–119, doi:10.1016/S0040-1951(03)00234-8, 2003.

Rapant, P., Struhár, J. and Lazeckỳ, M.: Radar interferometry as a comprehensive tool for monitoring the fault activity in the vicinity of underground gas storage facilities, Remote Sens., 12(2), doi:10.3390/rs12020271, 2020.

Roque, D., Perissin, D., Falcão, A. P., Fonseca, A. M. and Maria, J.: Dams regional safety warning using time-series insar techniques, Second Internatinal Dam World Conf., 21–24, 2015.

Sanabria, M. P., Guardiola-Albert, C., Tomás, R., Herrera, G., Prieto, A., Sánchez, H. and Tessitore, S.: Subsidence activity maps derived from DInSAR data: Orihuela case study, Nat. Hazards Earth Syst. Sci., 14(5), 1341–1360, doi:10.5194/nhess-14-1341-2014, 2014.

Tampuu, T., Praks, J., Uiboupin, R. and Kull, A.: Long term interferometric temporal coherence and DInSAR phase in Northern Peatlands, Remote Sens., 12(10), 7–9, doi:10.3390/rs12101566, 2020.

Tzouvaras, M., Danezis, C. and Hadjimitsis, D. G.: Small scale landslide detection using Sentinel-1 interferometric SAR coherence, Remote Sens., 12(10), doi:10.3390/rs12101560, 2020.

USGS: M 5.0 - 3 km NNE of Sidi Mérouane, Algeria, [online] Available from: https://earthquake.usgs.gov/earthquakes/eventpage/us6000bag6/executive (Accessed 26 June 2021a), n.d.

USGS: USGS Earthquake Hazards Program, [online] Available from: https://earthquake.usgs.gov/ (Accessed 26 June 2021b), n.d.

Wang, Z., Li, Z. and Mills, J.: A new approach to selecting coherent pixels for ground-based SAR deformation monitoring, ISPRS J. Photogramm. Remote Sens., 144, 412–422, doi:10.1016/j.isprsjprs.2018.08.008, 2018.

Wempen, J. M.: International Journal of Mining Science and Technology Application of DInSAR for short period monitoring of initial subsidence due to longwall mining in the mountain west United States, Int. J. Min. Sci. Technol., 30(1), 33–37, doi:10.1016/j.ijmst.2019.12.011, 2020.

WWO: Mila, Mila, Algeria Historical Weather Almanac, [online] Available from: https://www.worldweatheronline.com/mila-weather-history/mila/dz.aspx / (Accessed 26 June 2021), n.d.